A novel gaseus X-ray polarimeter: data analysis and simulation

R. Bellazzini[a], F. Angelini[a], L. Baldini[a], A. Brez[a], E. Costa[b], G. di Persio[b], L. Latronico[a], M. M. Massai[a], N. Omodei[a], L. Pacciani[b], P. Soffitta[b], G. Spandre[a]

[a]Istituto Nazionale di Fisica Nucleare - sezione di Pisa,
via Livornese 1291, I-56010 San Piero a Grado (PI), Italy
[b]Istituto di Astrofisica Spaziale del CNR,
via Fosso del Cavaliere 100, I-00133 Roma, Italy

ABSTRACT

We report on the development of a new highly efficient polarimeter, based on the photoelectric effect in gas, for the 2-10 keV energy range, a particularly interesting band for X-ray astronomy. We derive the polarization information by reconstructing the direction of photoelectron emission with a pixel gas detector. Attention is focused on the algorithms used in data analysis in order to maximize the sensitivity of the instrument. Monte Carlo simulation is also discussed in details.

Keywords: X-ray polarimetry, Gas detectors

1. INTRODUCTION

X-ray polarimetry is well established as one of the most interesting and promising sub-topics of X-ray astrophysics.[1] Nevertheless, due to limitations of the conventional techniques (Bragg diffraction at 45° and Thomson scattering at 90°), the experimental results are quite meager, consisting of just a single measurement (the Crab nebula case) that dates from 25 years ago.[2]

In order to meet the need of efficient instrumentation, we have developed a Micro Pattern Gas Detector[3] (MPGD) with pixel readout exploiting the photoelectric effect to derive polarization information. We let the radiation impinge on the detector orthogonally to it. When a photon is absorbed within the gas, a photoelectron is emitted; that happens preferentially in the plane orthogonal to beam axis (i. e. in the plane of the MPGD) and along the electric field vector of the photon itself. If the incoming radiation is linearly polarized, then, the azimuthal angle of emission ϕ (on the plane orthogonal to the direction of photon propagation) is not randomly distributed; actually, by working out the full calculation,[4] one find that, for a K-shell absorption, such a distribution is given by:

$$N(\phi) \propto cos^2\phi, \tag{1}$$

if the angle ϕ is measured starting from the direction of polarization of the incoming radiation. This dependence can be exploited for polarimetric applications, by means of photoemission direction reconstruction. The photoelectron interacts with the mixture leaving along its path ion-electron pairs; the released charge is amplified by a Gas Electron Multiplier[5] (GEM) and collected onto the readout plane by applying a suitable electric field.

In figure 1 two real tracks collected during tests with 5.9 keV unpolarized radiation are shown. In the energy range of our interest and in the used gas mixture tracks are typically few hundreds microns long; nevertheless, thanks to a finely segmented readout electrode, we are able to *resolve* them as real tracks and not as indistinct releases of charge. The charge release is clearly asymmetric, with an initial low ionization density evolving into a clear Bragg peak toward the end of the track, according to well known Bethe-Bloch formula:

$$\frac{dE}{dx} \propto \frac{Z}{E}. \tag{2}$$

Further author information: (Send correspondence to Luca Baldini)
Luca Baldini: E-mail: luca.baldini@pi.infn.it, Telephone: +39 050 880436, Address: via Livornese 1291, I-56010 San Piero a Grado (PI), Italy

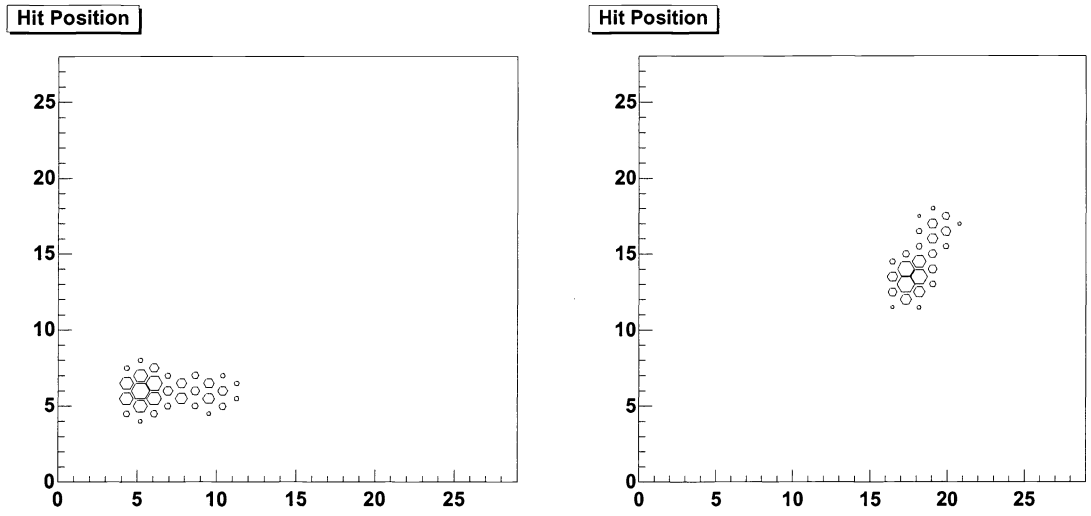

Figure 1. Two real tracks collected in a run with 5.9 keV unpolarized radiation; the area of each hexagon is proportional to the charge inducted on the corresponding pixel of readout plane. The gas mixture used is Ne/DME 80/20 at 1 Atm; since Ne K-shell is 0.9 keV, photoelectron energy is in this case 5 keV. Note that most of this energy is released in the Bragg peak toward the end of the path.

A littler excess of charge is also present at the beginning, due to the 0.8 keV Auger electron emitted as a consequence of atomic relaxation.

Photoelectron also suffers electromagnetic elastic collisions with nuclei which tend to drive it away from its original direction; this effect is responsible for a progressive randomization of the track direction. As a consequence the angular response of our device to 100 % linearly polarized radiation will not be given by the relation (1), but:

$$N(\phi) \propto C_1 + C_2 cos^2\phi, \tag{3}$$

in which the constant term C_1 takes into account the deterioration of angular information due to the Coulomb scattering. Starting from equation (3) we can define the so called *modulation factor*[6] μ, the standard parameter expressing instrument response to fully polarized radiation, which allows a direct comparison with other technologies:

$$\mu = \frac{C_2}{2C_1 + C_2} \Big|_{100\%\ polarised\ radiation}. \tag{4}$$

Finally, the modulation factor allows to evaluate the Minimum Detectable Polarization, which represents the real sensitivity of the device. It is defined as the minimum modulated flux necessary to exceed, at the desired level of confidence, the fluctuations of both the background and the unmodulated signal. It can be shown that MDP is given by[6]:

$$MDP(n_\sigma) = \frac{n_\sigma}{\varepsilon\mu F}\sqrt{\frac{2(B + \varepsilon F)}{ST}}, \tag{5}$$

where F is the source flux, ε the detection efficiency, B the background rate per unit of surface, S the collecting area and T the observing time; given a certain technology, equation (5) allows to evaluate the integration time necessary to perform a planned measurement.

2. DATA ANALYSIS

2.1. The basic reconstruction algorithm

The basic algorithm for the reconstruction of the track direction is based on the determination of the two (orthogonal) principal axes of the charge distribution. Once a reference system is somehow fixed on the readout

plane, starting from cartesian coordinates x_i and y_i of each fired pixel and from the signal Q_i collected on the corresponding electronic channel, the barycentre of the cluster can be easily calculated:

$$x_b = \frac{\sum_i Q_i x_i}{\sum_i Q_i},$$
$$y_b = \frac{\sum_i Q_i y_i}{\sum_i Q_i}. \tag{6}$$

From now on we fix the barycentre as the origin of our coordinates system (it can be simply done by the translation $x_i \rightarrow x_i - x_b$, $y_i \rightarrow y_i - y_b$). By rotating the reference system of an angle ϕ (figure 2), coordinates of each pixel transform as:

$$\begin{pmatrix} x_i'(\phi) \\ y_i'(\phi) \end{pmatrix} = \begin{pmatrix} cos\phi & sin\phi \\ -sin\phi & cos\phi \end{pmatrix} \begin{pmatrix} x_i \\ y_i \end{pmatrix}. \tag{7}$$

The second momentum of charge distribution (with respect to the barycentre) along a generic direction forming an angle ϕ with the original x axis can then be written as:

$$M_2(\phi) = \frac{\sum_i Q_i x_i'^2(\phi)}{\sum_i Q_i} = \frac{\sum_i Q_i (x_i cos\phi + y_i sin\phi)^2}{\sum_i Q_i}. \tag{8}$$

By imposing

$$\frac{\partial M_2(\phi)}{\partial \phi} = 0, \tag{9}$$

we obtain the two angles ϕ_{min} and ϕ_{max} (within the interval $[-\pi, \pi]$) for which the second momentum is respectively maximum and minimum:

$$\phi_{max,min} = -\frac{1}{2} arctan \left[\frac{2\sum_i Q_i x_i y_i}{\sum_i Q_i (y_i^2 - x_i^2)} \right]. \tag{10}$$

These angles can be substituted into equation (8) to work out the evaluation of the momenta themselves (M_2^{max} and M_2^{min}). From a physical point of view, the second momentum of the charge distribution along a certain

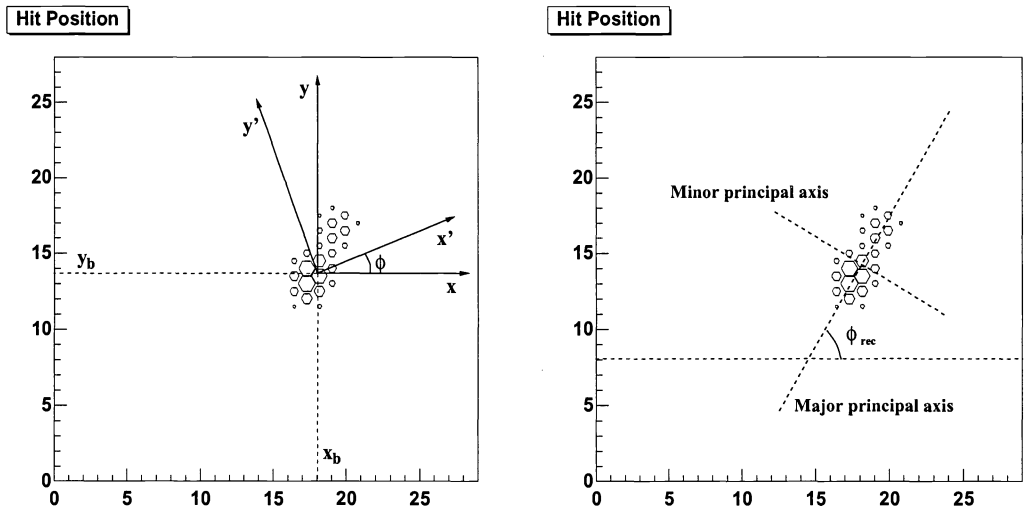

Figure 2. Definition of the general geometrical framework (left) and principal axes of charge distribution for a sample event (right). At the lowest order the reconstructed photoemission angle ϕ_{rec} can be identified with the direction of the major principal axis.

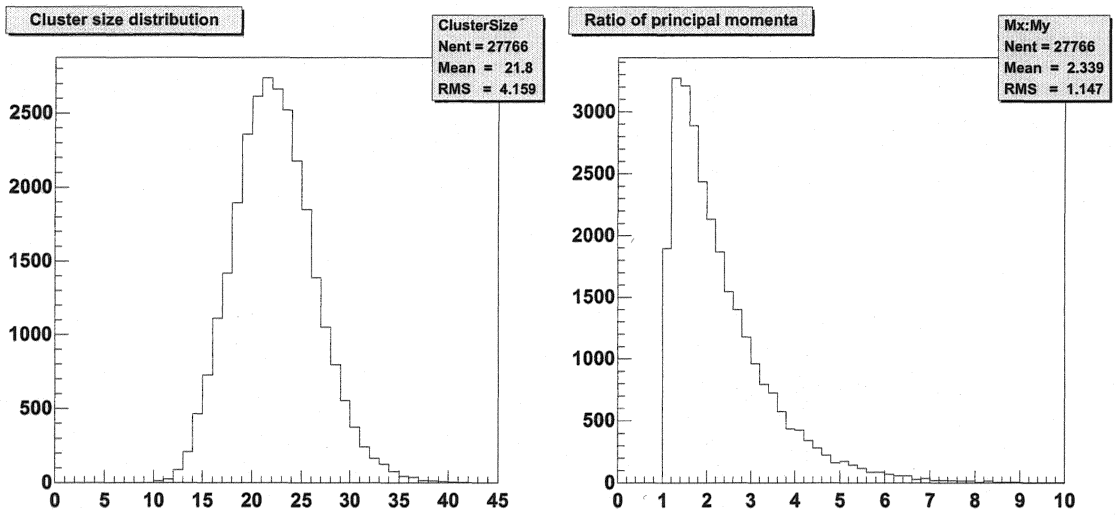

Figure 3. Number of fired pixels per event (left) and ratio of the principal second momenta of charge distribution ϵ (right), as obtained within a run with 5.9 keV unpolarized radiation. It is fundamental to note that most events are sensibly far from a spherical shape ($\epsilon = 1$), allowing an accurate angular reconstruction.

direction is directly correlated with the spatial extension of the track along the direction itself. In the case, for instance, of a simple elliptical distribution the quantities $\sqrt{M_2^{max}}$ and $\sqrt{M_2^{min}}$ are proportional to the major and minor semi-axes and the ratio M_2^{max}/M_2^{min} can be expressed in terms of the eccentricity e as:

$$\epsilon = \frac{M_2^{max}}{M_2^{min}} = \frac{1}{\sqrt{1-e}}. \tag{11}$$

We note that the large average number of fired pixels per event (figure 3) allows a good track reconstruction; in fact the distribution of the ratio M_2^{max}/M_2^{min}, confirms that most of the clusters are sensibly far from a spherical shape (in this case it would be quite difficult to assign them a direction).

At this level the reconstructed photoemission angle ϕ_{rec} can be identified with the angle indicating the major principal axis of the cluster, but it is important to remark that, so doing, the whole track is taken into account in the calculation, while we already know that most of the directional information resides into the initial part of the track, which is less randomized by Coulomb scattering. Results obtained following this approach with polarized radiation are quoted in figure 4. The cluster angular distribution is well described by the expression (3), peaked on the angle of polarization of incoming radiation. The analogous distribution, obtained with unpolarized photons, is clearly flat, confirming the absence of systematic effects. By applying a cut on the ratio of second momenta, the response modulation clearly increases (figure 4, center); while this feature is obviously not amazing (it simply means that longer cluster are better reconstructed) the matter is not so trivial as it could seem at a first sight. *Spherical* cluster (those who have a second momenta ratio not far from unity) basically derive from tracks much shorter than the average or from photoelectrons emitted with polar angle far from 90°, which is a depressed but allowed to occur event; in both cases a smaller readout pitch would increase the ratio between second momenta of such clusters, increasing the modulation factor as well. Moreover we note here that when the background is negligible if compared with source flux, that is quite a common case at the focus of a X-ray optics, MDP quoted in (5) scales as:

$$MDP \propto \frac{1}{\mu\sqrt{\varepsilon}}. \tag{12}$$

This means that for bright sources the leading parameter is the modulation factor; in this case suitable cuts on events, by increasing μ to the detriment of detection efficiency, could eventually produce a gain in sensitivity,

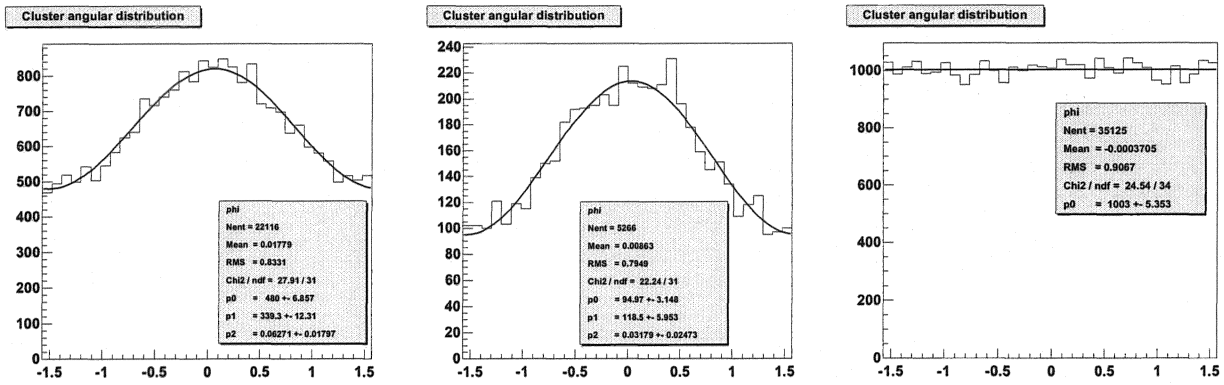

Figure 4. Response of MPGD to 5.4 keV linearly polarized radiation with no cuts on events (left) and applying the cut $M_2^{max}/M_2^{min} > 3$ (center); the fit, performed with the function $C_1 + C_2 cos^2(\phi - \phi_{rec})$ provides 26 % modulation factor in the first case and 39 % in the latter. This means that, as we expect, the reconstruction of the direction of emission is better for longer clusters. On the right, the photoelectron angular distribution in the case of 5.9 keV unpolarized X-rays is reported.

especially in the low energy limit, where tracks are shorter. An alternative approach, in order to preserve the detection efficiency, could be the application of a different statistical weight to the events in relation to the track length; in any case the definition of algorithms allowing the maximization of the instrument sensitivity, in its final configuration and in relation with physical target, will surely be one of the greatest efforts.

2.2. Conversion point reconstruction

At the lowest order, photon absorption point can be identified with the barycentre of the released charge; nevertheless a better reconstruction is fundamental not only in order to improve imaging capabilities of our instrument, but also because it could in principle allow to select the initial part of the track, which is less randomized by Coulomb scattering, improving angular reconstruction as well.

The leading idea, here, is that the initial part of the track is characterized by a lower ionization density, according to the Bethe-Bloch formula (2), as it can be clearly seen in sample events shown in figure 1. Since the parameter that measures the asymmetry of a distribution is the third momentum with respect to its barycentre, we calculate this quantity, for each cluster, along the major principal axis:

$$M_3 = \frac{\sum_i Q_i x_i'^3(\phi_{rec})}{\sum_i Q_i} = \frac{\sum_i Q_i (x_i cos\phi_{rec} + y_i sin\phi_{rec})^3}{\sum_i Q_i}. \tag{13}$$

The sign of M_3 basically tells us whether the Bragg peak of the track lies in the sense of positive or negative coordinates (along major principal axis) with respect to the barycentre. Once we have access to this information, a better guess of the photon conversion point can be obtained by simply projecting it back from the barycentre, along the principal axis of the cluster, by a distance d that can be chosen proportional to $\sqrt{M_2^{max}}$ (representing, at this stage, the *length* of our track). With respect to other possible choices, we have preferred to parameterize this distance as:

$$d = f(\epsilon)\sqrt{M_2^{max}}, \tag{14}$$

in which ϵ is the quantity defined in equation (11) and the function $f(\epsilon)$, of the order of unity, has been tuned on the collected data with the help of our Monte Carlo simulation (that will be discussed in the next section).

Results obtained by following this approach are reported in figure 5. They refer to a run with unpolarized X-ray radiation entering the detector through a narrow (50 μm diameter) collimator; in this case the conversion point is basically fixed, the dimension of collimator being much smaller than the pixel size. Barycentres of events tend to be distributed at some distance from the absorption point, verifying our interpretation that most

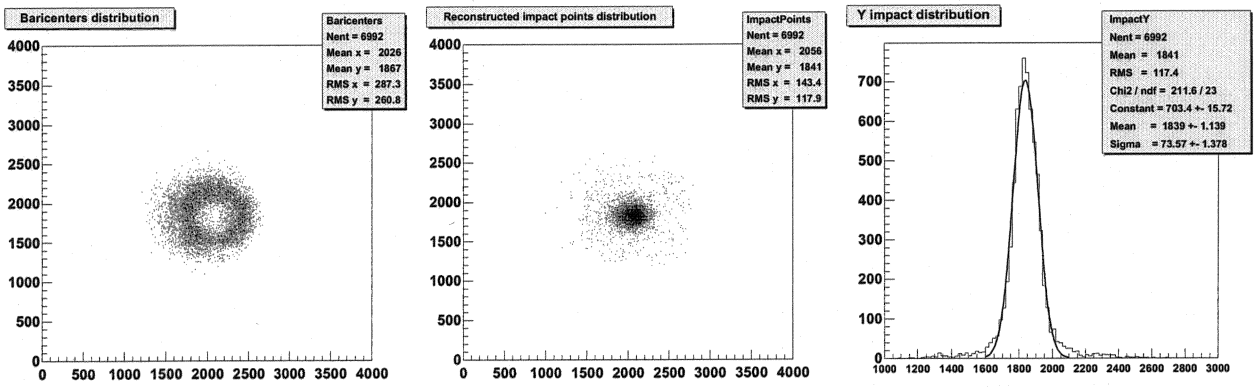

Figure 5. Distribution of barycentres (left), reconstructed conversion points (center) and one dimensional projection (right) referring to a run with point source (5.4 keV unpolarized radiation collimated within 50 μm); only events with $\epsilon > 2.5$ are shown. Note that standard deviation of the gaussian fit to reconstructed conversion points distribution is $\sigma \simeq 70 \mu m$, fixing the spatial resolution of our detector in present configuration.

of the charge is released toward the end of the track, while reconstructed conversion points are characterized by a much smaller distribution. The standard deviation of the gaussian fit to the reconstructed conversion points distribution is about 70 μm (figure 5, right); this value represents the spatial resolution of our detector in its present configuration, but it is clear that it could be largely improved by using a readout plane segmented with smaller pitch. With a pitch of 100 μm or 50 μm, which is probably not out of our reach, the MPGD could provide imaging capabilities not so far from a standard CCD camera.

Reconstruction of the absorption point is important non only to improve imaging capabilities of the instrument, but also to enhance accuracy in angular reconstruction. Since most of the directional information

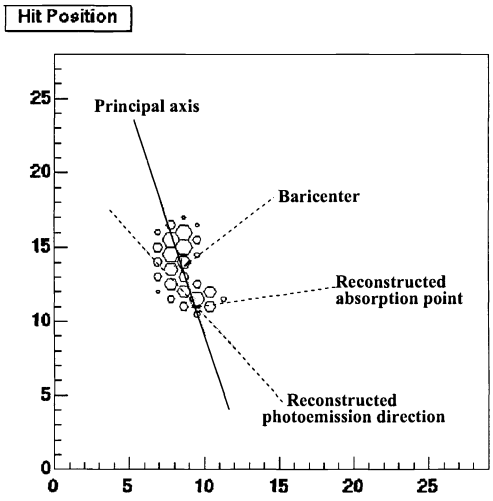

Figure 6. Reconstructed photoemission direction, as extracted by pixels which are close to the conversion point, can be sensibly different (and much more accurate) from principal axis of charge distribution.

resides in the initial part of the photoelectron track, once the conversion point has been estimated, the basic angular reconstruction algorithm can be applied again considering only fired pixels close to the conversion point

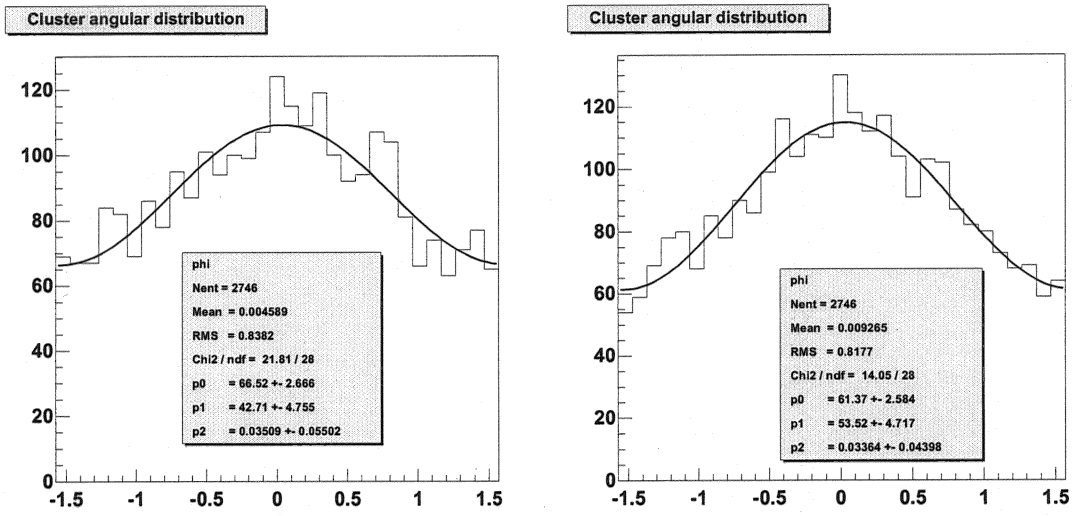

Figure 7. Distribution of principal axis directions (left) and photoemission directions reconstructed using conversion point information (right) within a run with 8 keV polarized radiation. The modulation factor rises up from 24 % to 30 %.

itself (figure 6); in this way the effect of the randomization induced in the final part of the track by Coulomb scattering on nuclei can be partially overcome. A more sophisticated approach, to be still investigated, could consist in weighting different pixels, within reconstruction, according to their distance from the reconstructed conversion point. It is clear that such a procedure can provide a significant improvement of accuracy only if the average number of fired pixel is large; that is, if tracks are much longer than readout pitch. It is also clear that, once the configuration of the detector is fixed, the algorithm works better at higher energies. Figure 7 shows the results for a run with 8 keV polarized radiation.

3. MONTE CARLO SIMULATION

3.1. The source code

The Monte Carlo simulation of the instrument basically involves the following steps:

- Simulation of photoelectron track and primary ionization distribution.
- Transverse diffusion and drift toward Gas Electron Multiplier.
- Gas amplification and transfer to read out plane.
- Electronic noise simulation and output data writing.

The simulation of photoelectron tracks (figure 8) has been carried out by means of SS_MOTT code,[7] which provides an accurate description of low energy electrons interaction. It performs a single scattering simulation using the Mott cross section and evaluates the energy lost between two subsequent elastic scatterings using a Bethe-Bloch formula modified to be valid in the keV regime. The azimuthal and polar emission angles are chosen according to the theoretical expression for photoelectric cross section:

$$\frac{d\sigma}{d\Omega} \propto \frac{sin^2\theta cos^2\phi}{(1-\beta cos\theta)^4}, \tag{15}$$

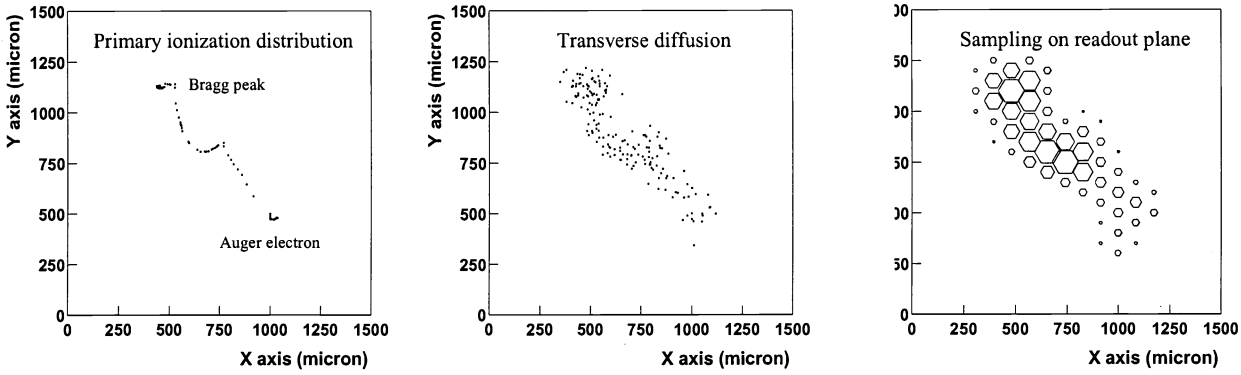

Figure 8. Simulated event referring to a 5.9 keV photon (absorbed in Ne) giving out a 5.0 keV photoelectron and a 0.9 keV Auger electron. Figure shows the distribution of primary ionization projected onto detector plane (left), the effect of the transverse diffusion over 5 mm drift length (center) and the corresponding track sampled on the readout plane (100 μm pitch) after GEM multiplication (right).

where β is the speed of the photoelectron (in terms of the speed of light). The distance z of the absorption point from the drift window is extracted following the usual distribution:

$$\frac{dn}{dz} = \lambda_a e^{-\frac{z}{\lambda_a}}, \tag{16}$$

where λ_a is the photon absorption length; expression (16) practically becomes a constant when the photon energy exceeds a few keV (in the limit of λ_a much greater than the gap thickness). Transverse diffusion of primary ionization can be parameterized with a gaussian distribution whose standard deviation is usually written, in terms of the drift length d and the diffusion coefficient D_t, as:

$$\sigma_t = D_t \sqrt{d}. \tag{17}$$

Since we are not interested in precise spectral response of the detector, we have chosen, for the GEM multiplication distribution, a pure exponential law, rather than a more complex formulation including *polya functions*:

$$P(n) = \frac{1}{\langle n \rangle} e^{\frac{n}{\langle n \rangle}}. \tag{18}$$

Electronic noise has been generated following a gaussian distribution for each channel also taking into account non uniformities within the readout plane. The output data format of the simulation is exactly the same as the real data, so that Monte Carlo simulations can be read with the same analysis program used for real data.

3.2. Results

In figure 9 some tracks produced by 5 keV electrons in pure Ne are shown; the blurring effect that Coulomb scattering produces on particles direction is clearly visible. It is noticeable that the modulation factor (figure 10), evaluated as a function of the distance from the absorption point, reaches values as high as 70 % (within 150 μm from the absorption point itself), clearly showing that we are not yet close to physical limitations and there is still space for great improvement (basically by means of a readout anode with smaller pitch).

Monte Carlo simulation is in good agreement with collected data in relation to all relevant parameters, such as pulse height, signal to noise, cluster size and principal momenta distributions. In figure 11 we report the simulated modulation factor, as a function of the photon energy, for the tested prototype, evaluated both with the basic algorithm and using the reconstructed absorption point information. Simulation suggests that, over a certain energy threshold, there is no more increase in the modulation factor by identifying the photoemission

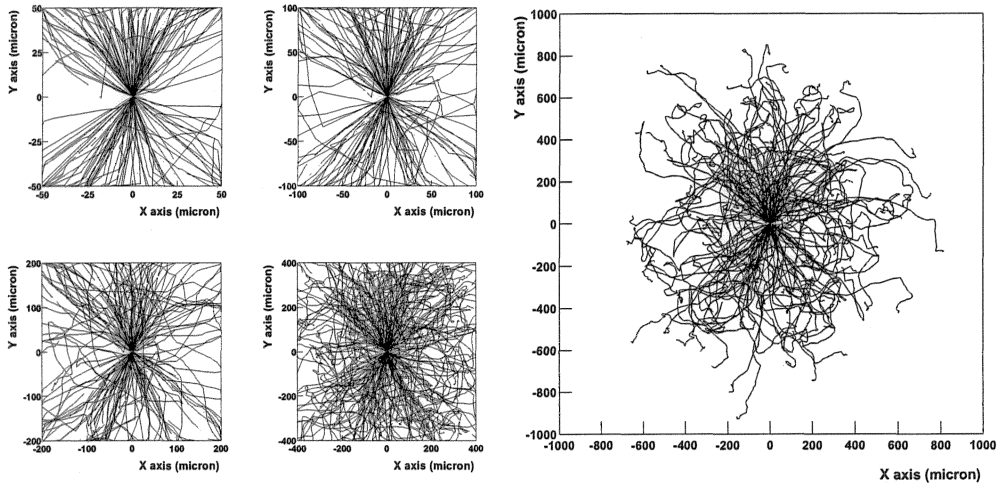

Figure 9. Simulated tracks (projected onto the detector plane) produced by 5 keV electrons in pure Ne, at pressure of 1 Atm (right). Starting directions are distributed according to equation (15), simulating photoelectrons emitted in response to a collimated, 100 % linearly polarized 5.9 keV photons beam. By means of a progressive "zoom out" (left), it can be clearly seen that the modulation of the track directions is more and more blurred by Coulomb scattering while going away from conversion point.

direction with the principal axis of the released charge distribution. At higher energy, in fact, tracks are longer and the probability for a large angle electromagnetic scattering to occur increases as well. On the other hand, a more sophisticated algorithm which isolates the initial part of the track (like the one we use) allows to efficiently overcome this limitation, as it is clearly confirmed by experimental data.

By means of our Monte Carlo code we have investigated the performance of a polarimeter with a 100 μm readout pitch (which is feasible with currently adopted technology and will be soon available for tests) for several

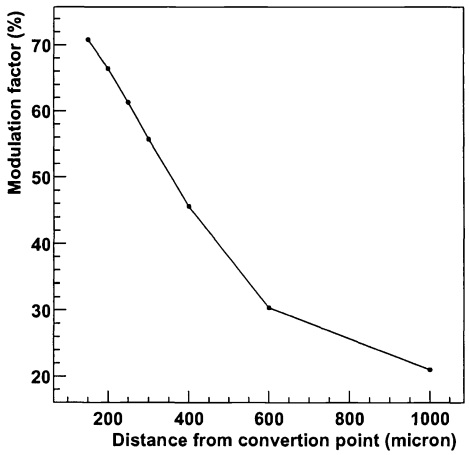

Figure 10. Modulation factor, as a function of distance from absorption point, evaluated from the distribution of primary ionization for 5 keV photoelectrons in pure Ne, 1 Atm.

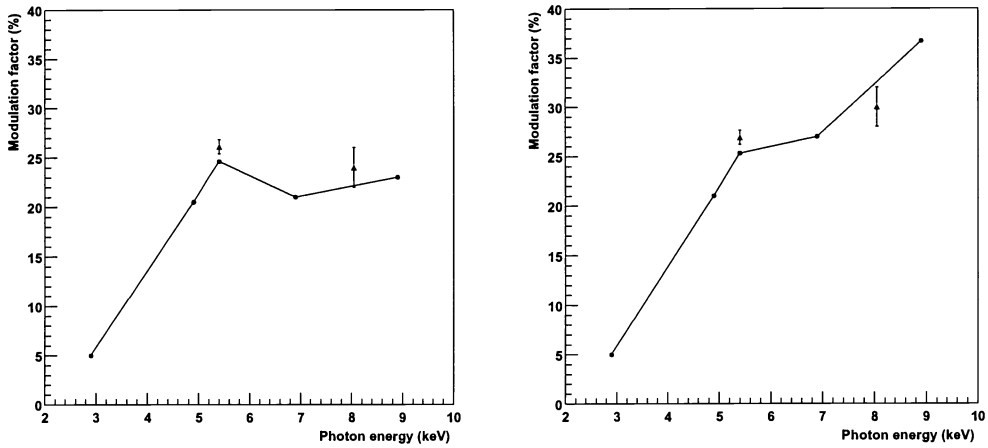

Figure 11. Modulation factor, as a function of photon energy, for the tested prototype, evaluated both with the basic algorithm (left) and exploiting reconstructed conversion point (right). Monte Carlo simulation (solid line) and experimental data (points with error bars) are reported.

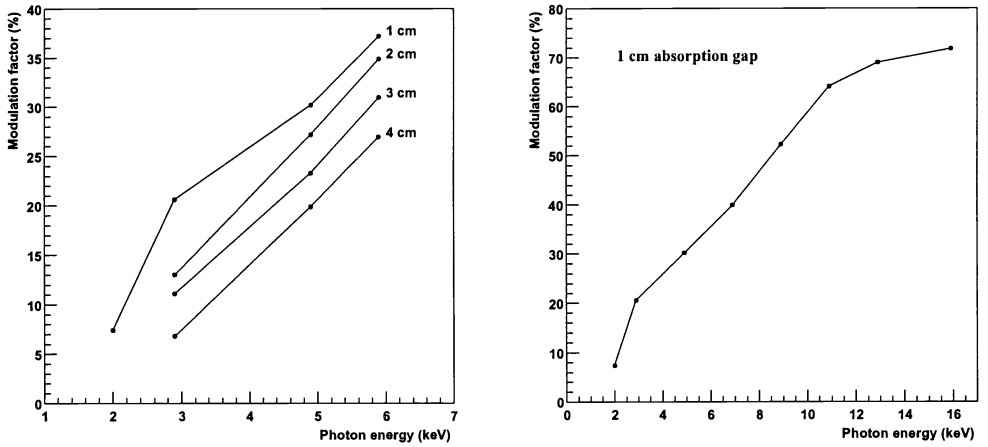

Figure 12. Modulation factor, as a function of photon energy, for a 100 μm readout pitch and different thicknesses of the absorption gap, ranging from 1 cm to 4 cm (left); complete energy scan for 1 cm absorption gap (right). In both cases the same gas mixture as the one used throughout our tests is assumed.

absorption gap thicknesses. Results are shown in figure 12 and demonstrate that great improvements over the current prototype are clearly possible. It is worth to note that, with 1 cm absorption gap, the instrument would be sensitive down to 2 keV, making this configuration particularly exciting, since in the low energy region spectra are more populated and X-ray optics very efficient.

4. CONCLUSIONS

The set of data presented in this paper constitutes a complete characterization of our instrument. We have discussed in details algorithms used within the analysis in order to maximize the sensitivity of the detector. Results of Monte Carlo simulation are also presented in details, and are in good agreement with collected

experimental data. They clearly show that, to date, we are mainly limited by the technology used for the read out plane, rather than by physics, suggesting that there is still room for significant improvements.

ACKNOWLEDGMENTS

This research is partially funded by Agenzia Spaziale Italiana (ASI).

REFERENCES

1. P. Meszaros, R. Novick, G. A. Chanan, M. C. Weisskopf, A. Szentgyorgyi, *Astrophysical implications and observational prospects of X-ray polarimetry*, The Astrophysical Journal, vol. 324, pp. 1056-1067, 1988.
2. M. C. Weisskopf, G. G. Cohen, H. L. Kenstenbaum, K. S. Long, R. Novick, R. S. Wolff, *Measurement of the X-ray polarization of the Crab Nebula*, The Astrophysical Journal, vol. 208, pp. L125-L128, 1976.
3. E. Costa, P. Soffitta, R. Bellazzini, A. Brez, N. Lumb, G. Spandre, *An efficient photoelectric X-ray polarimeter for the study of black holes and neutron stars*, Nature, vol. 411, pp. 662-664, 2001.
4. W. Heitler, *The Quantum Theory of Radiation*, Oxford University Press, 1970.
5. F. Sauli, *GEM: a new concept for electron amplification in gas detectors*, Nucl. Instr. Meth., volA. 386, pp. 531-534, 1997.
6. P. Soffitta, E. Costa, G. di Persio, E. Morelli, A. Rubini, R. Bellazzini, A. Brez, R. Raffo, G. Spandre, D. Joy, *Astronomical X-ray polarimetry based on photoelectric effect with microgap detectors*, Nucl. Instr. Meth., volA. 469, pp. 164-184, 2001.
7. D. C. Joy, *Monte Carlo Modeling for Electron Microscopy and Microanalysis*, Oxford University Press, Oxford, 1995.